

TWO-SCALE ANALYSIS OF MICROSCOPIC DAMAGE MECHANISMS AT EARLY STAGE OF FRACTURE PROCESS OF FERRITIC DUCTILE IRON BY MEANS OF COMPUTATIONAL MODELLING AND EXPERIMENTAL METHODOLOGIES

Diego O. Fernandino^a, Sebastián Toro^{b,c}, Pablo J. Sanchez^{b,c}, Adrián P. Cisilino^a and Alfredo E. Huespe^b

^a *INTEMA, CONICET/ UNMDP, Buenos Aires (ARGENTINA) (dfernandino@fi.mdp.edu.ar / cisilino@fi.mdp.edu.ar), <http://www.intema.gob.ar>*

^b *CIMEC, CONICET/UNL, Santa Fe (ARGENTINA) (storo@cimec.unl.edu.ar / ahuespe@intec.unl.edu.ar), <http://www.cimec.org.ar>*

^c *GIMNI-UTN-FRSF, Santa Fe (ARGENTINA) (psanchez@intec.unl.edu.ar), <http://extranet.frsf.utn.edu.ar/GIMNI>*

Keywords: Ductile iron, Damage mechanisms, Multi-scale analysis, Finite element, Mechanical testing

Abstract. In this work, a two-scale analysis to study the early stage of fracture process of ferritic ductile iron is presented. The methodology combines numerical analysis and exhaustive experimental observations in both macro and micro scales. The multi-scale problem is modeled using the pre-critical regime of the Failure–Oriented Multi-Scale Variational Formulation (FOMF), which is implemented via a FE² approach. Finite element analysis in the micro-scale is customized to account for plastic deformation and matrix-nodule debonding. Experiments in the micro-scale are used for microstructural characterization of the material mechanical properties and the assessment of the micro-scale plasticity/damage mechanisms; experiments in the macro-scale provide the data to calibrate and validate the methodology. The multi-scale model is found effective for capturing the sequence of events and extent of the plasticity/damage mechanisms in the micro-scale as well as to infer, via inverse analyses, the parameters of the matrix-nodule debonding law (fracture energy and peak tensile stress), which cannot be estimated through experiments. Results allow to draw conclusions related to the applicability of the FOMF and the RVE sizing for non-linear damage analysis. Additionally, it allows to develop new insights for the better understanding of ductile iron damage micromechanisms at early stage of damage.

1 INTRODUCTION

Ferritic Ductile iron (FDI) is a type of ductile iron (DI) materials whose microstructure consists in a ferritic metallic matrix with a uniform random distribution of nearly-spherical graphite nodules. The matrix solidification structure of DI consists of the “First To Freeze zones” (FTF), which are coincident with the axes and arms of the austenite dendrites, and the “Last To Freeze zones” (LTF), which result after the last portions of remaining melt between the solid phases. The influence of each microstructural variable on the macroscopic behavior of DI, in general, and FDI in particular, need to be characterized and identified.

In this sense, complementary to experimental work, computational mechanics emerges as a powerful tool to help to the better understanding of the effects of the microstructural features on the mechanical behavior of DI.

The present work focuses on homogenized multi-scale computational models. Multi-scale computational models are based on the concepts of homogenization and representative volume elements (RVE). The RVE provides the description of the material at the micro-scale, while the homogenization transfers the information from the micro to the macro-scale. Thus, the material response at the macro-scale results after the material behavior in the micro-scale and the model adopted for the homogenization. A very valuable and comprehensive description, in terms of the mechanical backgrounds and the variational foundations of this approach, can be found in the contributions by [Blanco et al \(2016\)](#).

The computational homogenization of the DI elastic response has been addressed by [Carazo et al. \(2014\)](#) and [Fernandino et al. \(2015\)](#). The paper by [Fernandino et al. \(2015\)](#) is a main antecedent for the present work. Among other results, they concluded that RVEs obtained from $100\times$ micrographs allow to compute homogenized Young’s modulus and Poisson’s ratios that differ less than 2% of the experimental values. However, the extension of elastic homogenization analyses to the elasto-plastic regime and the subsequent fracture process is a highly complex task due to the numerous nonlinear phenomena in the micro-scale: matrix yielding and softening, nodule debonding and crack nucleation and propagation.

As a first contribution towards the development of a multi-scale model that involves all DI failure phenomena, the present work concentrates in the analysis of the linear elastic and the early damage stages. The so-called early damage stage comprises the nodule debonding and distributed plasticity in the matrix. The methodology followed in this work is sketched in [Figure 1](#). It combines experimental and multi-scale computational analyses. The experimental analyses encompass micro and macro-scale tests. The purpose of the micro-scale tests is twofold: the mechanical characterization of FDI micro-constituents via instrumented nanoindentation tests, and the monitoring of damage evolution via optical and scanning electron microscopy (SEM). In the macro-scale, standard tensile tests are used to measure the stress (σ^{EXP}) vs. strain (ε^{EXP}) curve. The computational homogenization is performed using the pre-critical regime of the Failure–Oriented Multi-Scale Variational Formulation (FOMF) by [Sanchez et al. \(2013\)](#) and [Toro et al. \(2016\)](#). The FOMF is implemented via the FE analysis of a RVE specifically designed for capturing plasticity and material damage mechanisms. Micro constituent phases are endowed with phenomenological constitutive models based on the experimental observations and tests. The FOMF correlates the intrinsic complexity of the microstructural damage process with the material macroscopic behavior to provide the homogenized stress (σ^{HOM}) vs. strain (ε^{HOM}) response. The macro-scale response does not assume any a-priori material constitutive behavior, i.e. no phenomenological plastic law is assumed at the macro-scale.

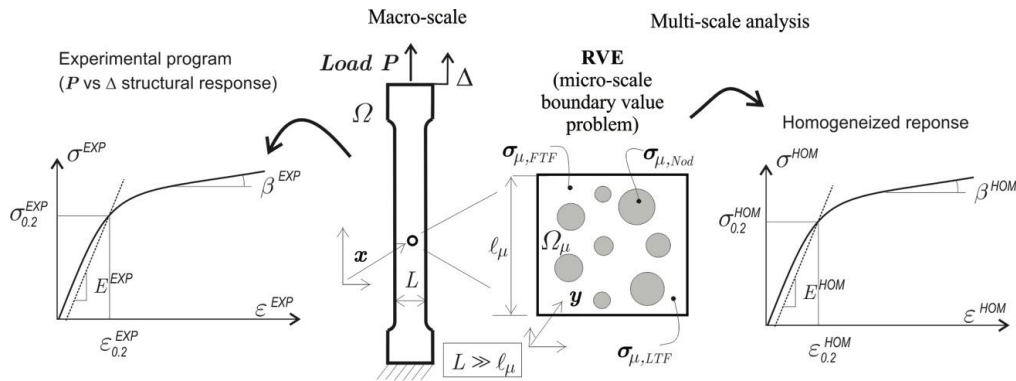


Figure 1: Experimental and computational multi-scale analysis methods. Mechanical quantities in the micro-scale are identified with the sub-index $[\cdot]_{\mu}$. Macro-scale quantities measured experimentally are identified with the supra-index $(\cdot)^{EXP}$, while those resulting from the computational homogenization procedure are denoted with the supra-index: $(\cdot)^{HOM}$

2 EXPERIMENTAL ANALYSES

2.1 Macro-scale experiments

The macroscopic material response was assessed via tensile tests. Five small-size round tension test specimens (ASTM E8M-04) were machined from one-inch-Y-blocks and tested according to the specifications of the ASTM A897M-03. As it is sketched in Figure 1, the P (load) vs. Δ (displacement) data was used to retrieve the σ^{EXP} vs. ε^{EXP} response. The result is in Figure 2, where the error bars indicate the dispersion of the five tests. The initial value for the Young’s modulus, E_0^{EXP} , and the offset yield stress and strain, $\sigma_{0.2}^{EXP}$ and $\varepsilon_{0.2}^{EXP}$, were computed from the σ^{EXP} vs. ε^{EXP} data using standard procedures. The hardening slope, β^{EXP} , was calculated as the best linear fit of the σ^{EXP} vs. ε^{EXP} data in the range $\varepsilon_{0.2}^{EXP} \leq \varepsilon^{EXP} \leq 1\%$, see Figure 3. The resultant values are $E_0^{EXP}=172 \pm 10$ GPa, $\sigma_{0.2}^{EXP}=275 \pm 8$ MPa, $\varepsilon_{0.2}^{EXP}=0.35 \pm 0.01$ % and $\beta^{EXP}=34 \pm 3$ MPa. It is emphasized that all measurements and calculations were made without assuming any a-priori material constitutive law.

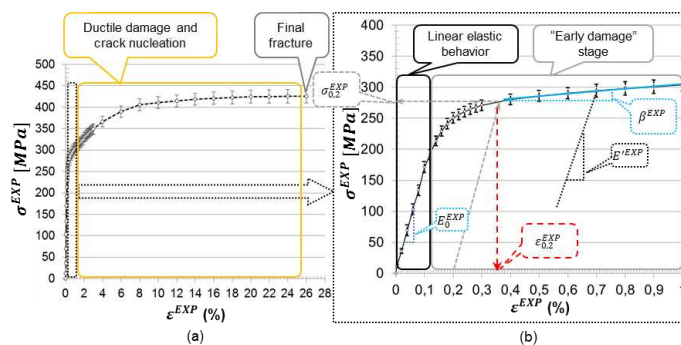


Figure 2: Measured σ^{EXP} vs. ε^{EXP} curve: (a) Complete deformation range up to failure, (b) Details with the linear elastic and early damage stages. Error bars indicate the dispersion of the experimental results. The chemical composition of FDI used is: 3.32%C, 2.36%Si, 0.03%Mg, 0.31%Mn, 0.62%Cu, and 0.02% Ni [%W]

2.2 Micro-scale experiments

2.2.1 Micrographic observations

Metallographic samples were prepared using standard polishing and etching methods. Following the same methodology reported in Fernandino et al. (2015), a color reagent

sensitive to microsegregation was used to reveal the FTF and LTF zones. Micrographs were obtained using an Olympus PMG3 optical microscope and digitally processed with Image Pro Plus software. The as-cast characterization according to ASTM A247 resulted in a pearlitic microstructure with an average nodule size of 6 (which corresponds to a maximum nodules size of about 40 μm), nodularity higher than 95%, nodular count of 100 nodules/ mm^2 and graphite area fraction of about 12%.

2.2.2 Failure mechanisms

Micrographic observations are correlated to the macroscopic σ^{EXP} vs. ε^{EXP} curves. Four stages are distinguished, see Figure 3:

- i. The linear elastic stage, which encompasses macroscopic strains $\varepsilon^{EXP} \leq 0.1\%$. In the micro-scale, graphite nodules remain bonded to the matrix, as it has been observed by [Fernandino \(2015\)](#).
- ii. The early damage stage, which involves the gradual Matrix-Nodule Decohesion (MND) and the localization of plastic strains that conducts to the formation of a plastic deformation band across the matrix. The initiation of MND is shown in Figure 3a and Figure 3b for macroscopic strains $\varepsilon^{EXP} \cong 0.18\%$ and $\varepsilon^{EXP} \cong 0.35\%$, respectively. The early damage stage encompasses macroscopic strains $\varepsilon^{EXP} \lesssim 1\%$.
- iii. Ductile damage and crack nucleation. Once the MND is completed, the plastic deformation band is the driving mechanism for the development of ductile damage ([Di Cocco et al. 2010](#)). Further load increments conduct to the nucleation of matrix cracks. [Figure 3c](#) and [Figure 3d](#) show highly-distorted nodular cavities that withstand $\varepsilon^{EXP} \cong 10\%$ and $\varepsilon^{EXP} \cong 18\%$.
- iv. Crack propagation and final fracture. Cracks propagate and they eventually coalesce into a single dominant crack that leads to the catastrophic material failure. The fracture surface exhibits a fully ductile fracture micromechanism with dimples and highly deformed nodule cavities. This is the failure mechanism usually reported for FDI under quasistatic loading conditions.

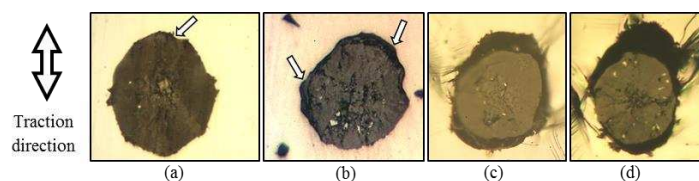


Figure 3: Optical micrographs of matrix-nodule interfaces at different strain levels retrieved from the conical specimen: (a) $\varepsilon^{EXP} \cong 0.18\%$, (b) $\varepsilon^{EXP} \cong 0.35\%$, (c) $\varepsilon^{EXP} \cong 10\%$ and (d) $\varepsilon^{EXP} \cong 18\%$. Arrows in (a) and (b) indicate the localization of matrix-nodule debonding

2.3 Micro-scale constituent characterization

The Young's modules $E_{\mu,Nod}$, $E_{\mu,FTF}$ and $E_{\mu,LTF}$ were measured using the well-known Oliver and Pharr method. Tests were practiced with a T1900 Hysitron equipped with a multi-range nanoprobe and a Berkovich indenter. Load control method was used; maximum load was set at 9500 μN . In order to avoid interferences among the plastically deformed zones of adjacent imprints, indentations were separated at least three-times the imprint size. The results for the Young's modules are summarized in [Table 1](#).

The FTF and LTF plastic properties were assessed by means of inverse FE analyses of nano-indentation data for the force vs. displacement records, plastic zone sizes and pile-up heights. FTF and LTF were assumed to have elasto-plastic J2 responses with isotropic exponential hardening. The yield surface is mainly characterized by the yield stress, while the

strain hardening is described through the dependence of σ_μ^y with the cumulative equivalent plastic strain, α_μ , as follows:

$$\sigma_\mu^y(\alpha_\mu) = \sigma_\mu^{y,0} + H_\mu \alpha_\mu + (\sigma_\mu^{y,\infty} - \sigma_\mu^{y,0}) [1 - e^{(-\delta_\mu \alpha_\mu)}], \quad (1)$$

where $\sigma_\mu^{y,0}$ is the initial yield stress of the pristine material, $H_\mu \geq 0$ is the linear hardening modulus, and $\sigma_\mu^{y,\infty} \geq \sigma_\mu^{y,0} \geq 0$ and $\delta_\mu \geq 0$ are material parameters. The inverse analysis for the determination of σ_μ^y , H_μ , $\sigma_\mu^{y,\infty}$, $\sigma_\mu^{y,0}$ and δ_μ , for the FTF and LTF zones, was developed in [Fernandino \(2015\)](#). The results for the plastic properties are summarized in [Table 1](#).

Constitutive model		Material constants					
		E_μ [GPa]	ν_μ	$\sigma_\mu^{y,0}$ [MPa]	$\sigma_\mu^{y,\infty}$ [MPa]	δ_μ	H_μ [MPa]
Nodule	Linear elasticity	15 ± 4	0.26	-	-	-	-
FTF	J2 elastoplasticity	212 ± 6	0.30	300 ± 15	540	20	180
LTF		239 ± 9	0.30	380 ± 18	710	20	260

Table 1: Material properties of the FDI micro-scale constituents.

3 MULTI-SCALE MODELING

In the present work, the FOMF is used to model the linear elastic and early damage stages of FDI failure process (stages i and ii in [Sections 2.3](#)). During these stages, the limit criterion that triggers the macro-scale instability (i.e. the nucleation of a macro-crack) is not achieved, and therefore, the FMOF reduces to a classical multi-scale homogenization technique. Modelling the damage stages (iii) and (iv) requires of more elaborated and unconventional multi-scale formulations.

For the present application, we adopt the notation $(\cdot)^{HOM}$ to label the effective macro-scale magnitudes that result from the FOMF homogenization. Both macro and micro-scale problems are solved using the two-dimensional plane-strain hypothesis. Additionally, macro and micro-scale kinematics are assumed to comply with the infinitesimal strain theory. However, it is important to note that for the general formulation of the FOMF, the infinitesimal strain assumption in the macro-scale does not impose restrictions to strain magnitudes in the micro-scale. The FOMF customizations for the FDI analysis are presented next. Details about the classical multi-scale model for FDI and their applicability limits for the proposed procedure can be found in [Fernandino et al \(2017\)](#).

3.1 Micro-cell finite element model for FDI micro-scale damage analysis

The problem at the micro-scale involves three material phases: the graphite nodules, the ferritic matrix, which includes the LTF and FTF zones and the matrix-nodule interface. Finite element meshes for the RVEs are illustrated in [Figure 4](#). Meshes are generated from micrographs. Mechanical properties of the phases are modeled as follows:

The Graphite nodules are assumed linear elastic and homogenous. Elastic constants are the Young's modulus, $E_{\mu,Nod}$, and the Poisson's ratio, $\nu_{\mu,Nod}$, which were determined experimentally (see [Table 1](#)). Bi-linear quadrilateral finite elements are used in the nodule discretization. The ferritic matrix is initially assumed as homogenous material (FTF zone properties). Then, the effect of incorporating the heterogeneous zones (LTF zones) in the macroscopic and microscopic response is reported in [Section 4.3](#). In all cases, the ferritic matrix is modeled using the same phenomenological elasto-plastic J2 law adopted in [Section 2.3](#) for its experimental characterization. Thus, Eq. (1) is specialized with the corresponding set of constants from [Table 1](#) depending whether the FTF or LTF zones are considered.

BBAR quadrilateral finite elements are used for the ferritic matrix (FTF and LTF zones). Matrix-nodule interfaces allow for the debonding mechanism between graphite nodules and the matrix. As it is shown in Figure 4c, the matrix-nodule interface are modelled using thin band-like domains, denoted as cohesive bands, inserted between nodules and matrix. Cohesive bands are of finite thickness, and so, they can be endowed with a regularized continuum constitutive law, such as a conventional damage model with elastic stiffness degradation. The elastic stiffness degradation only develops under tensile stresses and its development produces the characteristic exponential strain softening effect, which is typically observed in damage models. The details of the cohesive-band formulation can be found in Toro et al. (2016). The damage constitutive law is characterized by the Young's modulus, the Poisson's ratio, the critical stress, σ_μ^c , and the fracture energy, G_μ^f . The damage variable, d_μ , ranges from 0 to 1, where $d_\mu = 0$ indicates no damage and $d_\mu = 1$ indicates failure, this is, the complete loss of the element load-carrying capacity. Young's modulus and Poisson's ratio are assumed the same of the graphite nodules, $E_{\mu,MNI} = E_{\mu,Nod}$ and $\nu_{\mu,MNI} = \nu_{\mu,Nod}$. The values for σ_μ^c and G_μ^f could not be determined experimentally or found in the literature. So, they are left open for investigation in the next sections.

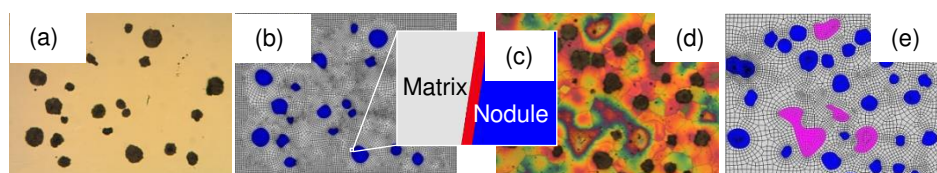


Figure 4: Finite element models at the micro-scale: (a) 100× micrograph, (b) Finite element mesh for a homogenous ferritic matrix (c) detail of the matrix-nodule interface, (d) 100× color-etched micrograph, (e) Finite element mesh for a heterogeneous ferritic matrix (FTF and LTF zones).

Following Fernandino et al. (2015), an RVE taken from a 100× micrographs of size 530 μm x 397 μm and containing 32 nodules is used for the micro-scale simulations. Finite element discretization of the RVE consists of 10393 quadrilateral elements with average size of 5 μm and cohesive band thickness of about 0.04 μm (additional details in Toro et al. 2016).

3.2 Cases of analysis

The computational multi-scale analysis consists of three cases: (i) Characterization of the matrix-nodule interface damage parameter: As it was reported in the previous section, the matrix-nodule interface critical stress, σ_μ^c , and fracture energy, G_μ^f , are the only micro-scale material parameters that could not be experimentally measured. Therefore, we estimate their values via inverse analysis. For the inverse analysis, a series of simulations for different combinations of σ_μ^c and G_μ^f are solved, and the pair (σ_μ^c, G_μ^f) that results in the best agreement between the simulation and the experimental data is identified. The series of multi-scale models combine increasing values of the critical stress $\sigma_\mu^c \geq 60$ MPa with fracture energies in the range $250 \text{ N/m} \leq G_\mu^f \leq 10000 \text{ N/m}$. The limiting values for the fracture energies are those of the graphite nodules and to the FTF zones, respectively (graphite and FTF fracture energy data are from Basso et al., 2009). The comparison between the simulation results and the experimental data is done in terms of macro-scale σ vs. ε responses and the evolution of the damage mechanisms in the micro-scale. Two limiting cases are solved to help assess the effects of nodules: (a) a porous material for which the graphite nodules are assimilated to voids, and (b) a material with perfectly bonded nodules. (ii) Verification of the RVE size: It is

worth to note that the RVE size here adopted is from the linear elastic analysis reported by [Fernandino et al. \(2015\)](#). Therefore, the suitability of the 100× RVE for the present non-linear damage case is verified. To this end, the independence of the multi-scale simulations is checked for larger micro-cell sizes. (iii) *Influence of LTF zones*: LTF zones are incorporated into the model to assess their influence on the material macro and micro-scale responses.

4 RESULTS

4.1 Characterization of the matrix-nodule interface damage parameters

4.1.1 Macroscopic response

[Table 2](#) shows a summary of the micro-scale cohesive band property data (σ_μ^c and G_μ^f) and their corresponding homogenized macroscopic results in terms of the offset yield strength and strain, $\sigma_{0.2}^{HOM}$ and $\varepsilon_{0.2}^{HOM}$, and stress-strain slope β^{HOM} in the hardening regime. Values of $\sigma_\mu^c < 120$ MPa and $\sigma_\mu^c > 180$ MPa are not reported because systematically underestimate and overestimate $\sigma_{0.2}^{HOM}$ and the post-yield stress level respectively.

Multi-scale analysis cases					
Micro-scale Cohesive band properties		Homogenized macroscopic results			
σ_μ^c [MPa]	G_μ^f [N/m]	$\sigma_{0.2}^{HOM}$ [MPa]	$\sigma_{0.2}^{HOM}/\sigma_\mu^c$	$\varepsilon_{0.2}^{HOM}$ [%]	β^{HOM} [MPa]
120	2500	269	2.24	0.332	14
	5000	271	2.26	0.334	34
140	2500	279	1.99	0.339	4
	5000	281	2.01	0.340	31
180	2500	298	1.66	0.351	21
	5000	299	1.66	0.350	23
Perfectly bonded nodules		296	-	0.356	100
Porous material		179	-	0.278	46

Table 2: Summary of the micro-scale cohesive band property data (σ_μ^c and G_μ^f) and their corresponding homogenized macroscopic results, $\sigma_{0.2}^{HOM}$, $\varepsilon_{0.2}^{HOM}$ and β^{HOM} . The experimental reference values are $\sigma_{0.2}^{EXP} = 275 \pm 8$ MPa, $\varepsilon_{0.2}^{EXP} = 0.35 \pm 0.01$ % and $\beta^{EXP} = 34 \pm 3$ MPa.

Similarly, values of $G_\mu^f < 2500$ N/m and $G_\mu^f > 5000$ N/m are not reported. It can be observed that $\sigma_{0.2}^{HOM}$ mainly depends on σ_μ^c . The best agreement between experiment, $\sigma_{0.2}^{EXP} = 275 \pm 8$ MPa, and numerical results is in the range $120 < \sigma_\mu^c < 140$ MPa. The interface fracture energy governs the post yield behavior. The values of $G_\mu^f = 5000$ N/m underestimates the post-yield stress level, irrespectively of σ_μ^c . This behavior is assimilated to a premature debonding of the nodule-matrix interface. Higher G_μ^f values systematically increment the post-yield stress levels; the limiting case is that of the perfectly bonded. The homogenized post-yield results are compared to those of the experiments by means of the stress-strain slope coefficient, β^{HOM} , which is computed as the best linear fit of the stress vs. strain data in the range $0.5 \% \leq \varepsilon^{HOM} \leq 1\%$. The results are also reported in [Table 2](#). Based on these analyses, it is concluded that $G_\mu^f = 5000$ N/m and $120 < \sigma_\mu^c < 140$ MPa (shaded entries in [Table 2](#)) are the combination of matrix-nodule interface damage parameters that produces the best agreement between the simulation results and the experimental data; the simulation results for the offset yield stress and the strain-strain slope in the hardening regime are within the dispersion of the experimental data. [Figure 5](#) shows the homogenized macroscopic material responses for these

damage parameters and the comparison with the experimental data retrieved from tensile test.

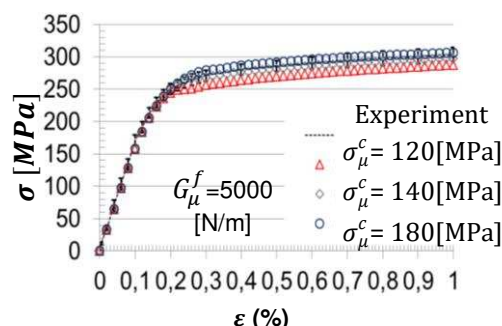


Figure 5: Homogenized macroscopic material responses for $G_\mu^f = 5000$ N/m. The black dashed lines are the experimental results; error bars indicate the experiment dispersion

4.1.2 Micro-scale response

Strain patterns and the matrix-nodule interface damage were monitored in the micro-scale to identify the homogenized stress and strain levels for which the MND and the plastic deformation band occur. The analyses were conducted for all the combinations of σ_μ^c and G_μ^f . Figure 6 shows the damage and plasticity evolution at the microstructural scale for the simulation with $\sigma_\mu^c=140$ MPa and $G_\mu^f=5000$ N/m. Table 3 compiles the results for the macro-scale stress and strain associated to the MND start, σ_s^{HOM} and ε_s^{HOM} , and end, σ_e^{HOM} and ε_e^{HOM} . In every case, the stress and strain results are normalized with respect to $\sigma_{0.2}^{HOM}$ and $\varepsilon_{0.2}^{HOM}$, respectively, in order to facilitate their correlation with the macroscopic material behavior.

σ_μ^c [MPa]	G_μ^f [N/m]	Nodule debonding start				Nodule debonding end			
		σ_s^{HOM} [MPa]	$\sigma_s^{HOM}/\sigma_{0.2}^{HOM}$	ε_s^{HOM} [%]	$\varepsilon_s^{HOM}/\varepsilon_{0.2}^{HOM}$	σ_e^{HOM} [MPa]	$\sigma_e^{HOM}/\sigma_{0.2}^{HOM}$	ε_e^{HOM} [%]	$\varepsilon_e^{HOM}/\varepsilon_{0.2}^{HOM}$
120	2500	256	0.95	0.22	0.66	268	1.00	0.35	1.04
	5000	259	0.96	0.23	0.69	273	1.01	0.36	1.08
140	2500	271	0.97	0.26	0.77	280	1.00	0.40	1.17
	5000	271	0.96	0.26	0.76	286	1.02	0.40	1.16
180	2500	291	0.98	0.31	0.88	303	1.02	0.54	1.54
	5000	293	0.98	0.33	0.93	313	1.05	0.54	1.54
140LTF	5000	272	0.97	0.26	0.76	295	1.04	0.42	1.23

Table 3: Stress and strain values for the matrix-nodule decohesion start and finalization.

It is observed that $\sigma_s^{HOM}/\sigma_{0.2}^{HOM}$ and $\varepsilon_s^{HOM}/\varepsilon_{0.2}^{HOM}$ primarily depend on σ_μ^c ; both increase with σ_μ^c . The ratio $\sigma_s^{HOM}/\sigma_{0.2}^{HOM} < 1$ irrespectively of σ_μ^c , i.e. debonding always starts before the material evidences yielding in the macro-scale. Debonding could finish either before or after yielding depending on σ_μ^c . Debonding finalization is also influenced by the fracture energy, the larger G_μ^f the longer it takes the debonding to complete.

The simulations that resulted in the best agreement between homogenized and experimental results ($120 < \sigma_\mu^c < 140$ MPa and $G_\mu^f = 5000$ N/m, see Section 4.1.1) predict the MND onset at $\sigma_s^{HOM}/\sigma_{0.2}^{HOM} \cong 0.96$. This is, MND starts just before yielding, without appreciable influence of σ_μ^c . On the other hand, the strain level for the MND onset presents a larger dispersion; its average value is $\varepsilon_s^{HOM}/\varepsilon_{0.2}^{HOM} \cong 0.73$. In what respects to the MND

finalization, it happens immediately after yielding at $\sigma_e^{HOM}/\sigma_{0.2}^{HOM} \cong 1.015$ and $\varepsilon_e^{HOM}/\varepsilon_{0.2}^{HOM} \cong 1.12$. As for the MND start, the strain value presents a larger dispersion than the stress one. The above results allow to hypothesize that the MND in FDI is intimately related to the material yielding. Note that the main variation of $\sigma_{0.2}^{HOM}$ is obtained as a consequence of variation in σ_μ^c , independently of the G_μ^f value (see Section 4.1.1).

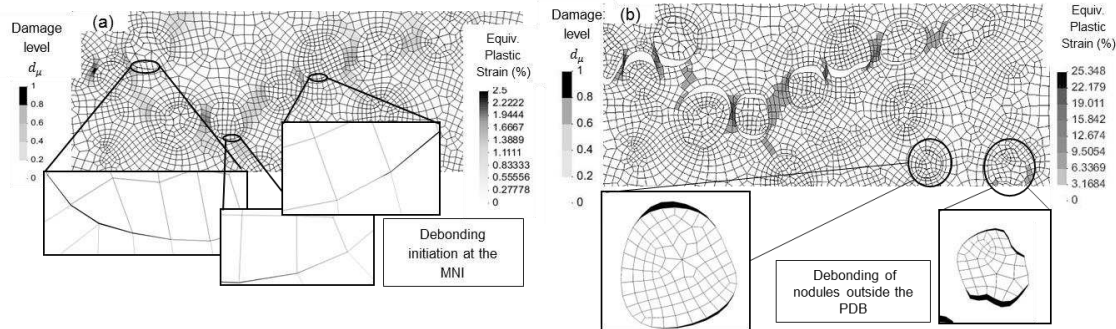


Figure 6: Damage and plasticity evolution at the microstructural scale for the simulation with $\sigma_\mu^c = 140$ MPa and $G_\mu^f = 5.000$ N/m: (a) onset of the nonlinear macroscopic response, $\varepsilon^{HOM} = 0.26\%$. (b) at $\varepsilon^{HOM} = 1\%$. Displacement fields are magnified 2x to better show the deboned zones.

4.2 RVE size verification

Results presented in Section 4.1 are outcomes of analyses performed using a single RVE geometry taken from a 100 \times micrograph. The suitability of the 100 \times -RVE for the non-linear regime is verified next. The simulation with $\sigma_\mu^c = 140$ MPa and $G_\mu^f = 5000$ N/m was performed four times using different 100 \times -RVEs and once using a 50 \times -RVE with 115 nodules. All numerical results lie within the dispersion of the experimental data and the values for 100 \times -RVEs exhibit a negligible dispersion. Based on the above results, it is concluded that 100 \times microstructural cell can be assimilated to an RVE for the analysis of the linear elastic and early damage stages. However, it will be necessary address the RVE sizing issue to model larger strain levels, say macroscopic strains $\varepsilon^{HOM} > 1\%$.

4.3 Influence of the LTF zones

LTF zones are incorporated into the models introduced in Section 4.2. Geometries of the LTF zones are taken from the micrographs, see Figure 4d-e. The material properties for the LTF zones are given in Table 1. The values for σ_s^{HOM} , σ_e^{HOM} , ε_s^{HOM} and ε_e^{HOM} that result from the simulations with the LTF zones are reported in Table 3; they are labeled as 140-LTF. It can be observed that the MND onset is not affected by the LTF zones, whereas the results for σ_e^{HOM} and ε_e^{HOM} in presence of the LTF zones are around 4% higher than those without the LTF zones. Based on these results, it is concluded that the LTF zones have not significant influence in the early damage stage. However, it is foreseen that LTF zones might play a key role on subsequent damage stages that involve higher levels of plastic strain and the nucleation and propagation of cracks.

5 CONCLUSIONS

The results allow for the development of new insights for the better understanding of the ductile iron damage mechanics, as for example:

- The formation of plastic deformation bands in the micro-scale reflects on the incipient linearity loss for the material response at the macro-scale.

- The nodule-matrix debonding can be described by a traction separation law that it is characterized in terms of the fracture energy, G_{μ}^f , and the critical stress, σ_{μ}^c . Estimated values, $G_{\mu}^f = 5000$ N/m and critical stress $120 < \sigma_{\mu}^c < 140$ MPa, are of the same order of those of the FTF and, consistently to the experimental observation in the micro-scale, they confer the matrix-nodule interface a weaker fracture resistance than that of the FTF-zones.
- In concordance with the experimental evidence, the multi-scale model predicts the occurrence of nodule-matrix debonding for nodules outside the plastic deformation band. These debonded interfaces do not take part of the final failure path, but it might be argued that their energy dissipation contributes to the overall material toughness.
- The last-to-freeze zones do not have a strong influence on the mechanical behavior during the early damage stage, but it is foreseen that they might play a key role on the subsequent damage stages, which involve higher levels of plastic strain, nucleation and propagation of matrix cracks.
- The early damage stage can be effectively modeled using infinitesimal strain formulations at the macro and micro scales. The modelling of the subsequent damage stages would require of a finite-strain formulation in the micro-scale to capture the strain localization within the plastic deformation band.
- Micro-cell finite element models constructed from $100\times$ micrographs and containing 32 nodules are representative volume elements for the analysis of the early damage stage.

REFERENCES

- Basso A., Martinez R., Cisilino A., Sikora J., Experimental and numerical assessment of fracture toughness of dual-phase austempered ductile iron. *Fatigue and Fracture of Engineering Materials & Structures* 33:1-11, 2009.
- Blanco P. J., Sánchez P. J., de Souza Neto E. A., Feijóo R. A., Variational foundations and generalized unified theory of RVE-based multi-scale models. *Arch. Comput. Methods Eng.* 23: 191–253, 2016a.
- Carazo F. D., Giusti S. M., Boccardo D., Godoy L., Effective properties of nodular cast-iron: A multi-scale computational approach. *Computational Materials Science* 82:378-390, 2014.
- Di Cocco V., Iacoviello F., Cavallini M., Damaging micromechanisms characterization of a ferritic ductile cast iron. *Engineering Fracture Mechanics* 77:2016–2023, 2010.
- Fernandino D. O., Cisilino A. P., Boeri R. E., Determination of effective elastic properties of ferritic ductile cast iron by means computational homogenization and microindentation test. *Mechanics of Materials* 83:110-121, 2015.
- Fernandino D. O., Fracture of ductile cast iron. Experimental analysis and multi-scale modelling. *PhD Thesis. National University of Mar del Plata*, March 2015. Mar del Plata, Buenos Aires, Argentina, 2015.
- Fernandino D. O., Cisilino A. P., Toro S., Sánchez P. J., Multi-scale analysis of the early damage mechanics of ferritic ductile iron. *International Journal of Fracture* 207:1–26, 2017.
- Sánchez P. J., Blanco P. J., Huespe A. E., Feijóo R. A., Failure-Oriented Multi-scale Variational Formulation: Micro-structures with nucleation and evolution of softening bands. *Comput. Methods Appl. Mech. Engrg.* 257: 221–247, 2013.
- Toro S., Sánchez P. J., Blanco P. J., de Souza Neto E. A., Huespe A. E., Feijóo R. A., Multi-scale formulation for material failure accounting for cohesive cracks at the macro and micro scales. *International Journal of Plasticity* 76: 75-110, 2016.